Extended Abstracts of the 2002 International Conference on Solid State Devices and Materials, Nagoya, 2002, pp. 476-477

P4-4

Structural and Electrical Properties of HfO_2-TiO_2 Composite Films Formed by Pulsed Laser Deposition

Kazutaka Honda, Satoru Goto, Mitsuo Sakashita, Hiroya Ikeda, Akira Sakai, Shigeaki Zaima[1] and Yukio Yasuda

Department of Crystalline Materials Science, Graduate School of Engineering, Nagoya University, Furo-cho, Chikusa-ku, Nagoya 464-8603, Japan
[1]Center for Cooperative Research in Advanced Science and Technology, Nagoya University,
TEL: +81-52-789-3819, FAX: +81-52-789-2760 E-mail: sakai@alice.xtal.nagoya-u.ac.jp

1. Introduction

Due to a reduction of device dimensions of metal-oxide-semiconductor field-effect transistors (MOSFETs), several problems araise in the SiO_2-based gate dielectric films. One of critical issues in thin SiO_2 films is the increased leakage current density due to the direct tunneling effect. One solution for this problem is to replace SiO_2 by high-dielectric-constant (high-k) materials. Large gate capacitance can be expected even in the thick films so that the direct tunneling of carriers is effectively suppressed. Required properties for the high-k gate insulator are a low leakage current property, high dielectric constant, high thermodynamic stability, and a low interface-trap density [1]. In particular, from the viewpoint of the leakage property, amorphous or single crystalline structures would be desired since grain boundaries act as an active leakage site [2-3].

In this work, we develop a growth process of HfO_2-TiO_2 composite films by using a pulsed-laser-deposition (PLD) method. The growth conditions for the formation of amorphous structures have been explored and polycrystalline structures consisting of μm-scale grains can be obtained by the solid phase growth using subsequent rapid thermal annealing (RTA). Correlation between the structural and electrical properties of the films is also examined.

2. Experimental

HfO_2-TiO_2 composite films were deposited by using PLD with HfO_2 and TiO_2 targets on Si (100) substrates treated by diluted HF. In this process, we employed stacking of thin HfO_2 and TiO_2 layers. Figure 1 shows two typical growth sequences during PLD. In the sample A, as shown Fig. 1(a), HfO_2 and TiO_2 layers, each of which was 0.6 nm in thickness, were alternatively deposited and nineteen layers were totally stacked. In the sample B, five layers consisting of 2.4-nm-thick HfO_2 and TiO_2 alternative layers were stacked, as shown in Fig. 1(b). The oxygen gas pressure during the deposition was 20 Pa and the substrate temperature was 400℃. Some samples were annealed by RTA at 700℃ for 30 sec in a nitrogen atmosphere.

X-ray diffraction (XRD) and transmission electron microscopy (TEM) were used to analyze the structural properties. Conducting atomic force microscopy (C-AFM) was used to observe the local leakage current distribution in the films.

3. Results and Discussion

Figures 2(a) and 2(b) show cross-sectional high-resolution (HR) TEM images of the sample A and B, respectively. Note that a homogeneous darker image is observed in the HfO_2 and TiO_2 deposited regions in the sample A, while darker and brighter stripes, corresponding to the HfO_2 and TiO_2 layers respectively, are clearly seen in the sample B. Close-up images in the insets in both Fig. 2(a) and 2(b) reveal that an amorphous structure was formed in the sample A while a polycrystalline structure in the sample B. These results indicate that the mixing of two materials as well as the amorphization occurs during the PLD process and thickness control of each layer is critical to grow the amorphous films.

Figure 3 shows a XRD profile of the sample A after RTA, which indicate that orthorhombic polycrystalline $HfTiO_4$ was grown and the grains were preferentially oriented to the [011] direction. A plan-view TEM image of the same sample is shown in Fig.4. It is observed that each grain has an elongated shape with a large size, typically of 200~400 nm in width and more than 1 μm in length. Furthermore, bend-contours, darker lines in the image, is clearly observed, which reflects the film structure consisting of strained grains.

Leakage current distribution of the RTA-treated sample A was also analyzed by C-AFM. Figures 5(a) and 5(b) show a topographic AFM image and a corresponding current image of the sample A after RTA, respectively. In the current image, brighter regions exhibit the sites with higher leakage current. It is found that the leakage current distribution is independent of the surface morphology but dark lines are frequently observed, as indicated by arrows in Fig. 5(b). From comparison between Fig. 4 and Fig. 5(b), we deduce that the leakage current distribution is influenced by the elongated grain structures of polycrystalline $HfTiO_4$.

4. Conclusions

We have explored growth processes of HfO_2-TiO_2 composite films, which allow us to obtain either an amorphous or a polycrystalline structure with large grains using PLD and subsequent RTA. The resultant film structure critically depends on the deposition sequence and amorphization of mixed HfO_2-TiO_2 phases was successfully demonstrated. Due to the solid phase growth of this amorphous phase by RTA, a polycrystalline $HfTiO_4$ film having larger grains with μm-scale size was grown. C-AFM analyses strongly suggest that the local leakage current distribution depends on the grain structures of polycrystalline $HfTiO_4$.

Acknowledgements

This work was partly supported by a Grant-in-Aid. for Scientific Research on Priority Areas (No. 13025226) from the ministry of Education, Culture, Sports, Science and Technology.

References

[1] G. D. Wilk, R.M. Wallace, and J. M. Anthony, J. Appl. Phys. **89**, 5243 (2001).

[2] K. Eisenbeiser, J. F. Finder, Z. Yu, J. Ramdani, J. A. Curless, J. A. Hallmark, R. Droopad, W. J. Ooms, L. Salem, S. Bradshaw, and C. D. Overgaard, Appl. Phys. Lett. **76**, 1324 (2000).

[3] G. D. Wilk, R.M. Wallace, and J. M. Anthony, J. Appl. Phys. **87**, 484 (2001).

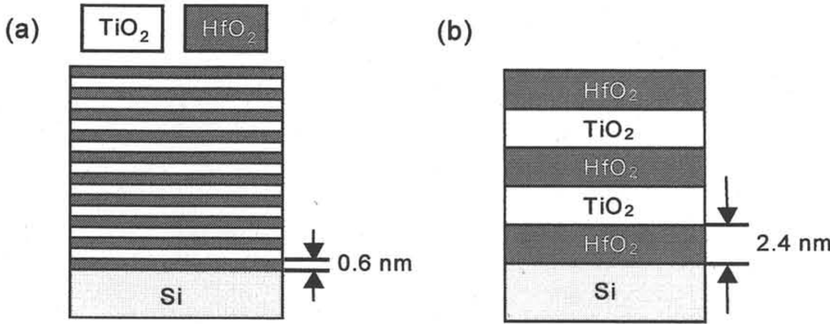

Fig. 1 The stacked structure of (a) the sample A and (b) sample B.

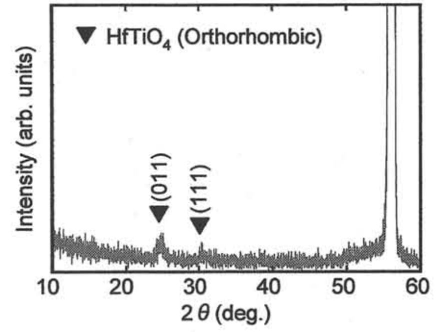

Fig. 3 XRD profile of the sample A after RTA.

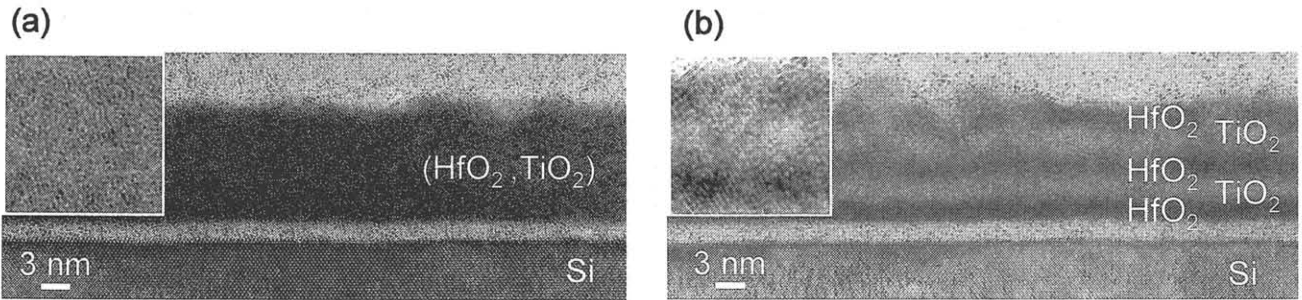

Fig. 2 TEM images of (a) the sample A and (b) the sample B deposited at 400℃.

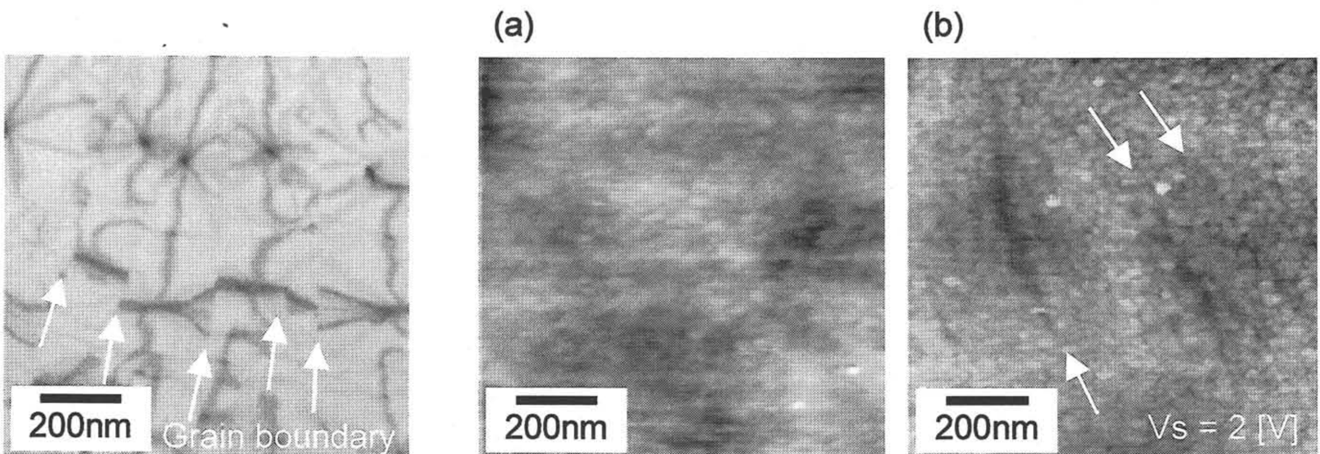

Fig. 4 Plan-view TEM image of the sample A after RTA. Fig. 5 (a) Topographic AFM image and (b) corresponding current image of the sample A after RTA.